STUDY ON THE UTILIZATION OF TIO₂/NISE/N/C FOR CR(VI) PHOTOREDUCTION

Elfirza Zain[a], Yuly Kusumawati[a*], Saepurahman[b]

[a]Department of Chemistry, Faculty of Science and Data Analytics, Institut Teknologi Sepuluh Nopember, Kampus ITS Keputih, Sukolilo, Surabaya 60111, Indonesia

[b]Research Center for Chemistry, National Research and Innovation Agency (BRIN), Gd. 452 KST BJ Habibie Serpong, Tangerang Selatan, Banten 15314, Indonesia

Graphical abstract
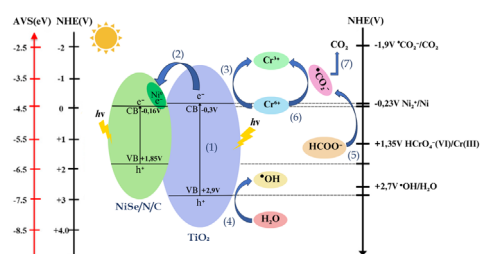
Abstract

The toxic contaminant chromium is commonly found in industries such as electroplating, metallurgy, and metal processing. Cr(VI) ions are highly toxic, carcinogenic, and mutagenic. Photocatalytic reduction has emerged as a promising method for Cr(VI) removals due to its high efficiency, cost-effectiveness, and the absence of secondary pollutants. TiO_2 was chosen as a photocatalyst due to its exceptional photocatalytic activity. However, TiO_2 has the disadvantage of a broad bandgap and rapid electron-hole recombination. To overcome this drawback, a heterojunction is formed between TiO_2 and NiSe. Nevertheless, TiO_2/NiSe suffers from poor thermal stability and a tendency to agglomerate. To address these issues, NiSe is modified using carbon and nitrogen materials derived from chitosan. In this research, TiO_2/NiSe modified with N/C has been synthesized through the solvothermal method as a photocatalyst utilizing two forms of TiO_2, namely rutile (Rk) and P25 (Pk). The resulting photocatalysts are optimized for reducing Cr(VI) in water through photocatalysis. X-ray diffraction (XRD), Field Emission Scanning Electron Microscopy (FESEM), UV-Diffuse Reflectance Spectroscopy (UV-DRS), and Fourier Transform Infrared (FTIR) spectroscopy were utilized for characterization. The UV-Vis DRS analysis indicated a reduction in the bandgap upon incorporating carbon and nitrogen elements. Rutile TiO_2's bandgap has decreased from 3 eV to 2.87 eV, while P25 TiO_2's bandgap has decreased from 3.14 eV to 3.04 eV. The photoreduction study of TiO_2/NiSe/N/C in water against Cr(VI) was also conducted with several variations, namely light source (no light, TL lamp, 365 nm lamp, 254 nm lamp) and hole scavenger (formic acid). The photoreduction test results demonstrate the superior performance of the composite compared to pure TiO_2. For example, under 254 nm light, the P25 sample significantly improved from 20.41% (P) to 53.26% (Pk). The Rk sample shows the strongest activity in TL light, which achieved a photoreduction rate of up to 48%. The best photoreduction study results were obtained by the Pk sample at 254 nm lamp variation using a formic acid hole scavenger with 99.7% photoreduction.

Keywords: Clean water, Cr(VI), formic acid, hole scavenger, photoreduction, TiO_2

1.0 INTRODUCTION

Modern industrial processes, fueled by the continual integration of emerging technologies, have resulted in dramatic developments in the industrial sector. These advances, however, have resulted in an unprecedented environmental calamity. The unregulated release of industrial effluents into aquatic ecosystems, subterranean aquifers, and terrestrial water bodies has contaminated these reservoirs with various harmful contaminants [1], [2]. Chromium, a heavy metal, is particularly problematic among these contaminants [3]. Harmful chromiums are mostly from industrial sectors such as electroplating, metallurgy, textiles, tanning, and metal processing [4].

In aquatic environments, chromium primarily occurs in two oxidation states: trivalent chromium (Cr(III)) and hexavalent

chromium (Cr(VI)). Cr(VI) is highly toxic, surpassing Cr(III) by an order of magnitude, and recognized to be carcinogenic and mutagenic to environmental and human health [5], [6]. As a result, many countries require that Cr (VI) concentrations in wastewater be reduced to less than 0.05 mg/L before being released into water sources [7].

Adsorption, coagulation, flocculation, precipitation, membrane filtration, and reduction are among some techniques proposed for chromium removal [8]–[10]. Adsorption readily removes Cr(VI), however adsorbent saturation demands replacement or extra treatment. Furthermore, the desorption of adsorbed Cr(VI) can result in secondary waste. Similarly, secondary waste is produced in the form of coagulants or flocs by the particle aggregation processes of flocculation and coagulation. Precipitation, while facilitating the separation of solids, can also produce toxic sludge, a type of secondary waste [9], [11]. Photoreduction, by directly converting Cr(VI) to the less toxic Cr(III) without reliance on additional chemical precipitation, offers a highly efficient and cost-effective solution for Cr(VI) removal with minimal to no secondary waste generation. This process stands out for its remarkable effectiveness and environmental friendliness, positioning photocatalytic reduction as a promising solution [12], [13].

The photocatalytic process begins when a semiconductor absorbs photons surpassing its bandgap's energy. This causes electrons in the valence band to move to the conduction band, generating electron-hole pairs. These photogenerated electrons and holes can react with oxygen (O_2) and water (H_2O) in the atmosphere, forming powerful radicals like hydroxyl and superoxide anions. These radicals, along with the transfer of electrons directly to Cr(VI) ions, facilitate a series of redox reactions leading to the reduction of Cr(VI) to its less toxic form, Cr(III). These radicals possess the ability to break down bacterial structures, neutralize viruses, and participate in reactions with organic compounds, yielding carbon dioxide and water as the final product [14]–[16].

It is important to note that the photocatalytic reduction of Cr(VI) typically proceeds slowly due to the inherent slow kinetics of water-to-oxygen reduction [17]. Introducing hole scavengers during the Cr(VI) photoreduction process, on the other hand, can significantly accelerate the reduction kinetics [18], [19]. Titanium dioxide (TiO_2) is a widely used material in photocatalysis. This choice is based on TiO_2's exceptional photocatalytic activity, favorable chemical properties, excellent stability, and low cost. At pH 5.6, TiO_2 has a bandgap of about 3.2 eV, with a conduction band around -0.3 eV and a valence band around +2.9 eV. As a result, Cr(VI) with a reduction potential more positive than -0.3 eV can undergo reduction via the photogenerated electrons. Meanwhile, water and organic pollutants undergo oxidation, directly or indirectly through the photogenerated holes [20].

However, titanium dioxide (TiO_2) has its drawbacks, most notably its broad bandgap of 3.2 eV and prevalent photocatalytic activity in the ultraviolet (UV) wavelength range [21]. Addressing these constraints is critical for ensuring effective reactions under visible light conditions, given that the majority of natural light Earth receives is visible light (39%) yet only a tiny fraction of Ultraviolet light (5%) [22]. Furthermore, TiO_2's reduced photocatalytic efficiency can be credited to the fast recombination of electron and hole pair, in which electrons become trapped within holes, limiting their ability to facilitate the photocatalysis process [23], [24].

As a result, ongoing research aims to modify and improve TiO_2's photocatalytic performance. Diverse approaches for the modification and augmentation of TiO_2 have been explored and documented, encompassing techniques such as doping, surface alteration employing inorganic acids, and the formation of heterojunctions. Among these methods, heterojunctions have emerged as particularly efficacious, as they hold the potential to simultaneously reduce the bandgap of TiO_2 and curb the recombination of e^--h^+ pairs [25]. The concept of heterojunctions can be further categorized into two classes: those utilizing precious metals and those employing semiconductors. Recent investigations have unveiled that introducing noble metals into the crystal structure of wide bandgap semiconductors like TiO_2 can markedly augment the photocatalytic performance in the visible light spectrum, owing to the effect of surface plasmon resonance associated with noble metals [26]. Nonetheless, due to their scarcity and exorbitant cost, the practical application of precious metals on an industrial scale is fraught with impracticality [27].

Another notable method is the fabrication of heterojunction semiconductors by combining semiconductors with metals or other semiconductors with compatible band energy levels. The formation of such heterojunctions able to promote charge carrier separation and boost the photocatalytic activity of the catalyst [28]. To that end, a diverse array of co-catalysts based on transition metals has been employed to fabricate heterojunction semiconductors. Nickel (Ni) is a particularly promising candidate among these metal-semiconductor because of its low cost, commendable photocatalytic activity, and natural abundance [29]. NiSe, one of its compounds, has gotten a lot of attention due to its diverse potential applications in conductivity, optics, magnetism, and catalysis. A study to incorporate NiSe into a TiO_2 heterojunction semiconductor has been conducted by [27]. The results reveal that NiSe incorporation can reduce the TiO_2 bandgap to 3.15 eV. Nonetheless, the TiO_2/NiSe combination, particularly pure NiSe, has drawbacks such as poor thermal stability, agglomeration, and a scarcity of active sites [27].

Considering these shortcomings, dedicated research has been conducted to resolve them. A recent study used carbon and nitrogen materials derived from peptone to modify NiSe successfully. This modification reduced agglomeration while increasing conductivity and thermal stability [30]. In this study, chitosan, chosen for its accessibility and affordability compared to peptone, is investigated as a source material for carbon and nitrogen materials. These components are utilized to synthesize a TiO_2/NiSe/N/C photocatalyst via the solvothermal method. Notably, it also introduces a distinctive variety by incorporating two TiO_2 variants, rutile and P25, in the synthesis process. The study assesses the photocatalytic efficiency of the TiO_2/NiSe/NC material in chromium photoreduction under varied experimental conditions, such as light intensities and hole scavenger.

2.0 METHODOLOGY

2.1 Materials and methods

Sodium selenite (Na_2SeO_3 99.5%), rutile TiO_2 99.5%, Degussa P25 TiO_2 99.5%, Potassium dichromate ($K_2Cr_2O_7$ 99%), Nickel(II) nitrate hexahydrate ($Ni(NO_3)_2.6H_2O$ 99.9%), 1,5-diphenylcarbazide 98%, deionized water, formic acid 98%, ethanol 99.9%, acetone 99.8%, ethylenediamine 99%, and H_2SO_4 99.9% were purchased from Merck Group. Chitosan was synthesized in the Material and Energy Chemistry Laboratory, Department of Chemistry, ITS. Ethylene glycol 99.5% was supplied by OCI. None of the materials were further purified before usage.

The procedure described in [30] was used to synthesize Ni/N/C and NiSe/N/C, which is illustrated by the first and second row of Figure 1. Initially, 15 mL of deionized water was used to dissolve 0.4 grams of $Ni(NO_3)_2 6H_2O$. Subsequently, 1 gram of chitosan is introduced. The mixture is then stirred and ultrasonicated for 30 minutes. The resulting mixture was then heated for six hours at 220°C in a Teflon-lined autoclave for a hydrothermal process. Once cooled to room temperature, the samples were dried overnight in an oven at 80°C after being rinsed with ethanol and deionized water. The solids were then carbonized at a heating rate of 7°C per minute in a tube furnace with a nitrogen gas atmosphere. The result of this process was labeled as Ni/N/C.

Na_2SeO_3 powder (0.0691 grams) was dissolved in a solution of 10 mL ethylene glycol and 20 mL ethylenediamine. The mixture was then stirred for another 20 minutes. Following that, 0.07 grams of previously prepared Ni/N/C were introduced. The resulting mixture was then heated for six hours at 160°C in a Teflon-lined autoclave for a solvothermal process. Once cooled to room temperature the samples were rinsed with ethanol and deionized water and dried for 12 hours in an oven at 60°C. The product derived from this process was labeled as NiSe/N/C. The TiO$_2$/NiSe/N/C synthesis followed the methodology described in [27], which is illustrated on the last row of Figure 1. In a beaker containing 40 mL of ethylene glycol, 0.4 grams of TiO$_2$ powder and

0.06 grams of previously synthesized NiSe/N/C powder were dissolved. The resulting mixture was then heated for 24 hours at 180°C in a Teflon-lined autoclave for a solvothermal process. After allowing the samples to cool, the samples were washed with ethanol and deionized water and then left to dry in the oven for 12 hours at 60°C. TiO$_2$/NiSe/N/C was the product derived from this step. It should be noted that TiO$_2$ variants, specifically TiO$_2$ rutile and TiO$_2$ P25, were used in the synthesis process.

2.2 Characterization

The testing using X-ray diffraction (XRD) was done on a PW 3040/60 X'Pert Pro instrument set to 40 kV and 30 mA with a Cu K radiation source (Kα=1.54060) and a 2θ range of 5-90°. The Field Emission Scanning Electron Microscopy-Energy Dispersive X-ray spectroscopy (FESEM-EDS) was done utilizing the JIB-4610F instrument to examine samples' structure, morphology, particle size, and elemental distribution. UV-Diffuse Reflectance Spectroscopy (UV-DRS) was used with a Cary 60 spectrophotometer to examine the optical bandgap and light absorption properties of samples between 200 and 800 nm. The FTIR (Fourier Transform Infrared) Spectroscopy was used to identify the functional groups that were present in samples using a Shimadzu IR Prestige 21 instrument in the 200-800 nm range.
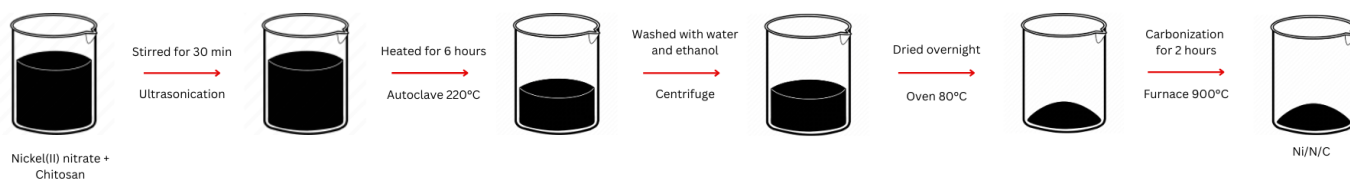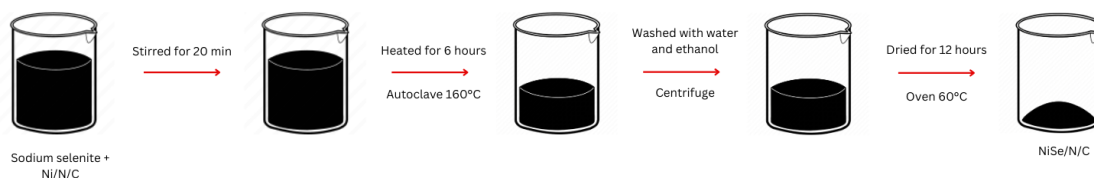
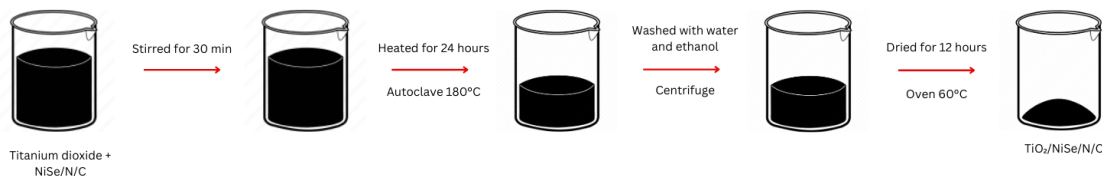**Figure 1.** TiO$_2$/NiSe/N/C synthesis schematic

Table 1 Variations for Cr(VI) Photoreduction with TiO2/NiSe/N/C

Photocatalyst	Hole scavenger	Sample's name	Light source (nm)
TiO₂ (rutile)	-	R	
	Formic acid	R-af	
TiO₂/NiSe/N/C (rutile)	-	Rk	
	Formic acid	Rk-af	TL/365/254
TiO₂ (P25)	-	P	
	Formic acid	P-af	
TiO₂/NiSe/N/C (P25)	-	Pk	
	Formic acid	Pk-af	

2.3 Photocatalytic Reduction of Cr(VI)

Initially, 20 mg of TiO₂/NiSe/N/C were dissolved in 20 mL of Cr(VI) 50 ppm solution. The solution is treated ultrasonically for 10 minutes. In some variations, 200 µl of hole scavenger were incorporated. Inside a chamber box, the solution was stirred for 1 hour while exposed to a light source with a fixed distance of 14.5 cm between the solution and the lamp. Three variations of the light source are used in this research: TL, 365 nm, and 254 nm. In addition, a control variation involving no light exposure was carried out. After 1 hour, a 2 mL sample was extracted for subsequent centrifugation, allowing the photocatalyst powder to be separated from the photoreduced chromium solution. Table 1 provides a detailed explanation of all the variations in this study.

The Cr(VI) removal percentage was assessed utilizing the Diphenyl carbazide (DPC) method. Photoreduced chromium solution (1 mL) was carefully transferred into a 100 mL volumetric flask. Subsequently, H₂SO₄ 6N was added to adjust the pH to 1 ± 0.3. The flask was filled with deionized water to bring the total volume to 100 mL. Following this, 2 mL of the DPC solution was introduced. The flask was vigorously shaken and left to react for 10 minutes. The absorbance was assessed using a UV-Vis Spectrophotometer at 540 nm. The percent reduction of chromium (VI) was calculated using Equation 1, where A_0 is the absorbance before the photoreduction process and A_1 the absorbance after the photoreduction process.

$$\text{Cr(VI) removal (\%)} = \frac{(A_0 - A_1)}{A_0} \times 100\% \qquad (1)$$

3.0 RESULTS AND DISCUSSION

3.1 Characterization of TiO₂/NiSe/N/C

The synthesis of Ni/N/C and NiSe/N/C closely followed the methods outlined in [30], resulting in black solids. The synthesis of TiO₂/NiSe/N/C solids described in [27] yielded whitish-gray (Rk) and blackish-gray (Pk) solids. The crystallographic properties of samples are investigated using X-ray diffraction (Figure 2 (a)). Diffractogram analysis of sample P reveals distinct peaks at 25.2°, 37.6°, 48.06°, 53.81°, 54.99°, and 62.67° that correspond to the interplanar planes (101), (004), (200), (105), (211), and (204). These peaks correspond to the TiO₂ anatase phase (JCPDS 21-1272). Another peak at 27.4 corresponds to the plane (110) of rutile TiO₂ (JCPDS 21-1276). For sample Pk, similar peaks can be seen. Meanwhile, there are several peaks at 27.25°, 35.99°, 41.20°, 54.25°, and 56.45° from samples R and Rk that can be indexed to the (110), (101), (111), (211), and (220) planes corresponding to rutile phase (JCPDS 21-1276). This result validates the TiO₂ phase's integrity before and after synthesis [31]. In the case of the NiSe/N/C sample, five NiSe peaks can be seen at 29.55°, 32.79°, 44.28°, 44.39°, and 51.66° (JCPDS 65-3425). Pk and Rk both contain identical peaks. Broad and weak peaks at 25° can be found in all samples indicating amorphous carbon structure [32].

In the FTIR spectrum as shown in Figure 3, characteristic peaks for Ti-O are observed at 491.46 cm⁻¹ for sample R. Identical peaks can be found for samples P, Pk, and Rk. Bonds between nickel and selenide and Ti-O-Ti can be found in the range of 600-700 cm⁻¹. Characteristics peaks that show the bending and stretching vibration of the hydroxyl group can be seen in 1636.41 cm⁻¹ and 3357.71 cm⁻¹ for sample R. Identical peaks can be found in samples P, Pk, and Rk. At 1058.58 cm⁻¹ and 1091.81 cm⁻¹ a C-N bond can be observed for samples Pk and Rk [33]–[36].
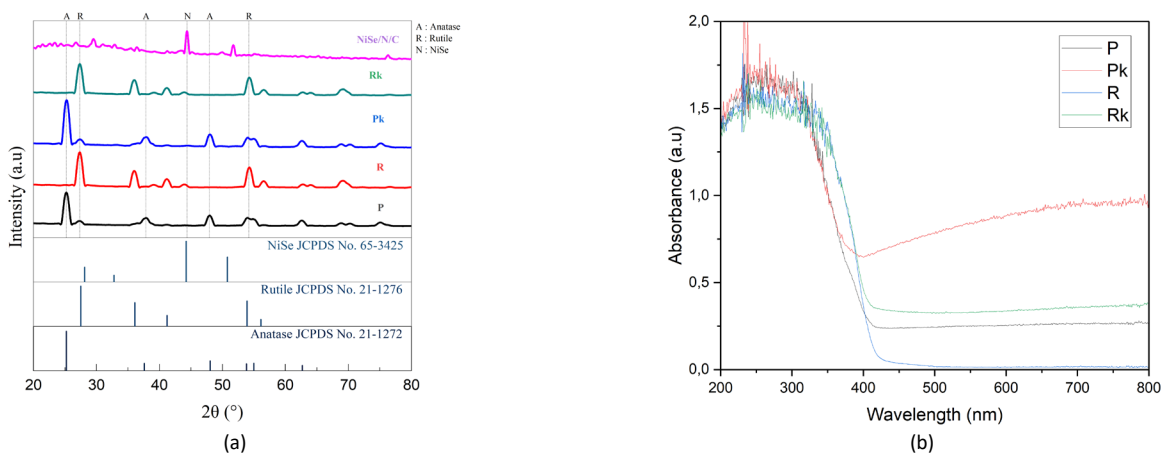
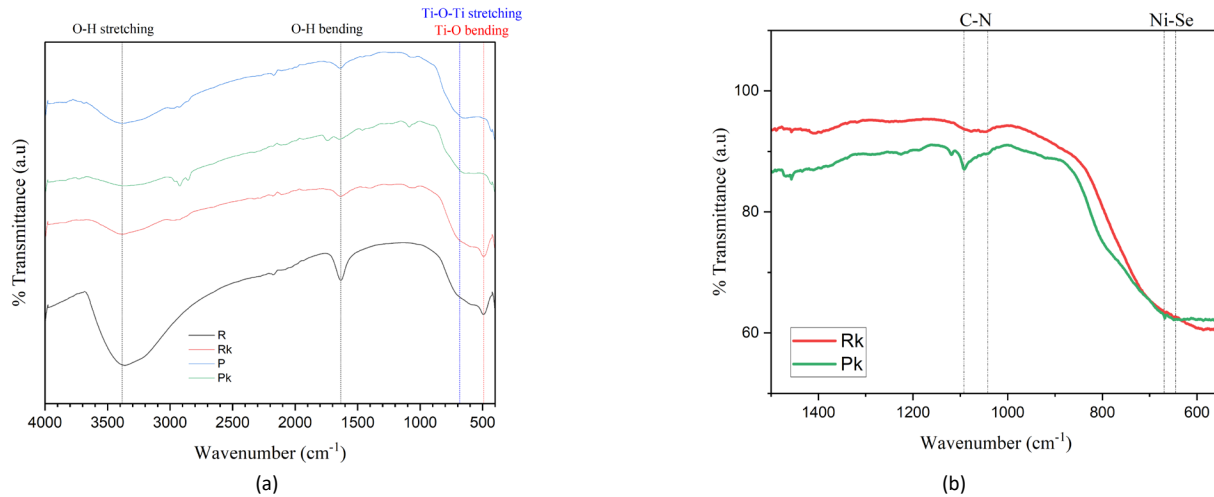**Figure 2.** Diffractogram of NiSe/N/C, P, Pk, R, Rk (a) and absorbance of P, Pk, R, Rk (b)

Figure 3. FTIR Spectra of P, Pk, R, Rk showing TiO2 functional group (a), NiSe and C-N functional group (b)

UV-DRS characterization results indicate high UV absorbance (Figure 2 (b)) for all samples. Bandgap energies, calculated using the Tauc Plot method, are 2.87 eV (Rk), 3 eV (R), 3.14 eV (P), and 3.04 eV (Pk), corresponding to wavelengths of 432 nm (Rk), 414 nm (R), 395 nm (P), and 407 nm (Pk). This shows that the proposed method successfully decreases the bandgap energy of TiO_2 (Figure 5).

FESEM characterization reveals the tetragonal structure of NiSe within TiO_2/N/C, with particle diameters of 41.5 nm (TiO_2/N/C) and 558 nm (NiSe) for the Pk sample and 68.43 nm (TiO_2/N/C) and 1077 nm (NiSe) for the Rk sample. These FESEM characteristics are described by Figure 4, where (a) is for sample Pk and (b) for Rk. The agglomeration of NiSe particles arises due to inadequate dispersion during the synthesis process. To achieve uniform particle dispersion, ultrasonication is employed, with the duration of ultrasonication directly affecting the reduction of agglomeration and particle size. The optimal ultrasonication time varies depending on the particle type and size. In the present study, unlike NiSe, the precursor utilized for TiO_2 synthesis possesses a nano size. Consequently, a more prolonged ultrasonication period is required during the NiSe synthesis stage compared to TiO_2 [37].
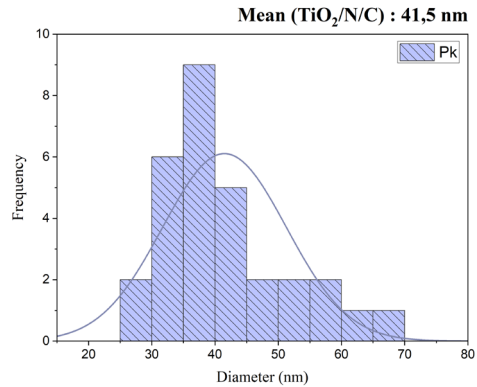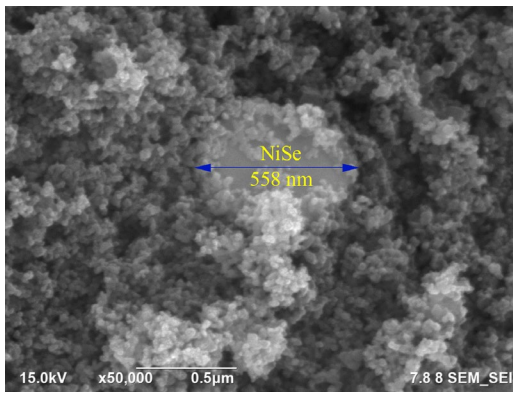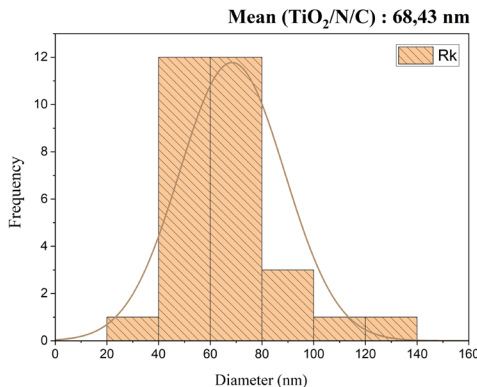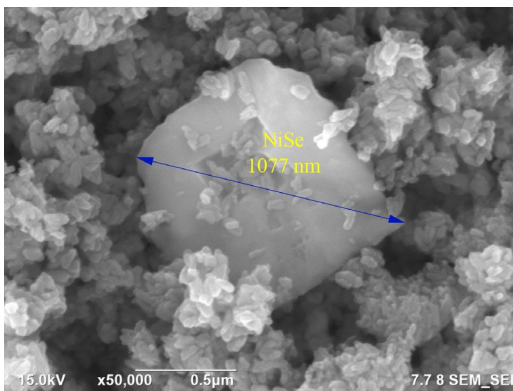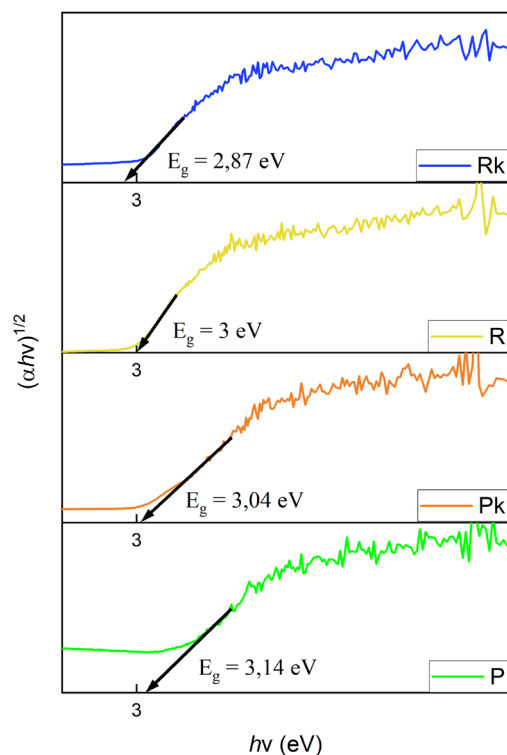

Figure 4. FESEM image of sample Pk (a), and Rk (b)

Figure 5. Bandgap energy of samples P, Pk, R, Pk

3.2 Photocatalytic Reduction of Cr(VI)

Cr(VI) photoreduction activity was assessed for TiO$_2$/NiSe/N/C P25 and TiO$_2$/NiSe/N/C rutile photocatalysts (Table 2). No significant Cr(VI) reduction occurred with no light, ruling out adsorption mechanisms. Then, under various lamps, the composite showed more Cr(VI) reduction compared to pure TiO$_2$. The Pk sample showed a notable increase from 20.41% to 53.26% under 254 nm light. The formic acid hole scavenger led to Cr(VI) reduction exceeding 97% under 254 nm and 365 nm lamps, with the P sample achieving the highest reduction percentage at 99.73%. TiO$_2$ rutile (R and Rk) samples exhibited enhanced activity under TL lamps due to their smaller bandgaps. Meanwhile, P and Pk show better activity under UV light (254 and 365 nm) due to the TiO$_2$ precursor chosen for the sample. P25 is more reactive than rutile because, in contrast to

rutile, it has a higher capacity for adsorbing hydroxyl groups and a decreased rate of charge carrier recombination [38], [39].

Before the photocatalytic activity began, the combined solution of Cr(VI) and photocatalyst had a pH of 5.6. Because of this, two forms of Cr(VI), namely HCrO$_4^-$ and Cr$_2$O$_7^{2-}$, can coexist throughout the photoreduction process [40]. When exposed to Cr(VI) in an acidic environment, diphenylcarbazide demonstrates astounding sensitivity and specificity [41]. A pink-colored chromophore formed by the chelation of Cr(III) with diphenylcarbazone is created as a result of this interaction. In this process, Cr(VI) causes the oxidation of diphenylcarbazide, creating a chelate between diphenylcarbazone and chromium [42]. The molecular formulas (Figure 6) of diphenylcarbazide and diphenylcarbazone are represented as H$_4$L and H$_2$L, respectively, with the following reactions taking place [16].

$$2CrO_4^{2-}{}_{(aq)}+ 4H_4L_{(aq)}+ 8H^+{}_{(aq)} \rightarrow 2[Cr(III)(H_2L)_2]^+{}_{(aq)} + 8H_2O_{(l)} \quad (2)$$
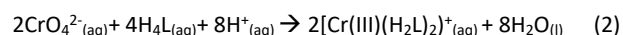
3.3 Possible Photocatalytic Reaction Mechanism

The suggested mechanism for the reduction of Cr(VI) by TiO$_2$ and TiO$_2$/NiSe/N/C is as follows. The photocatalyst produces holes in the valence band (VB) and electrons in the conduction band (CB) when exposed to light with an energy level higher than its bandgap energy (VB). TiO$_2$'s point of zero charge (pzc) is approximately six, corresponding to Ti^{IV}-OH [43]. As a result, the TiO$_2$ surface adopts a positive charge as Ti^{IV}-OH$_2^+$ when the pH drops below this level. According to estimates of Cr(VI) species at pH 5.6, the hexavalent chromium's main chemical species is HCrO$_4^-$.

Electrostatic interaction between nanosized HCrO$_4^-$ and TiO$_2$ species encourages Cr(VI) to adhere to the TiO$_2$ surface. TiO$_2$, which is nanosized, has a sizable surface area. Additionally, under acidic conditions, the presence of protons further augments this adsorption process. Furthermore, by directly reacting with the produced electron radicals, the adsorbed Cr(VI) can be easily reduced to Cr(III) [16]. Similar to pure TiO$_2$, when exposed to radiation, TiO$_2$/NiSe/N/C causes the surface of both TiO$_2$ and NiSe/N/C to produce pairs of holes and electrons simultaneously. The internally generated electric field of TiO$_2$ and NiSe allows for the quick passage of electrons from TiO$_2$'s conduction band to NiSe at their interface [44].

Table 2 Results of Cr(VI) photoreduction activity test on samples R, Rk, P, and Rk

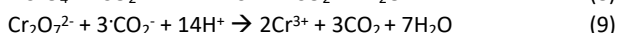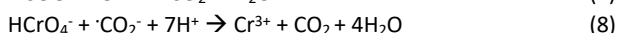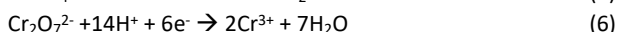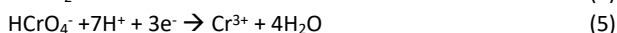| Photocatalyst	Sample's name	Percent Photoreduction (%)			
		No light source	TL	365 nm	254 nm
TiO$_2$ (*Rutile*)	R	0,25	3,67	9,27	4,04
	R-af	2,61	46,81	99,35	99,18
	Rk	0,58	8,58	16,26	10,38
TiO$_2$/NiSe/N/C (Rutile)	Rk-af	5,05	48,03	99,33	99,08
TiO$_2$ (P25)	P	1,99	3,01	11,59	20,41
	P-af	0,40	18,79	99,73	99,38
	Pk	4,76	3,80	17,21	53,26
TiO$_2$/NiSe/N/C (P25)	Pk-af	9,71	22,72	97,61	99,70

Figure 6. Molecular structure of diphenylcarbazide (a), diphenylcarbazone (b) [40]

TiO_2 has a conduction band potential that is more negative (-0.31V) compared to Ni^{2+}/Ni (-0.23V) reduction potential. As a result, NiSe is partially reduced to NiO metal, which occurs when photoexcited e^- from the TiO_2 conduction band transfers onto the NiSe co-catalyst. A Schottky barrier could be formed at the Ni/TiO_2 interface, where electrons from TiO_2 accumulate on the metal side [45]. Charge carrier recombination in TiO_2 is significantly reduced due to this occurrence, making it easier for electrons to move smoothly from TiO_2 to NiSe and Ni^0 metal [27].

Formic acid also makes it possible to scavenge the hydroxyl radicals (·OH) produced by the reaction between holes and OH^-. This reaction produces reactive $·CO_2^-$, with a notably lower redox potential (E^0 ($·CO_2^-/CO_2$) = -1.9 V vs NHE) as opposed to the redox potential of Cr(VI) (E^0 ($HCrO_4^-/Cr^{3+}$) = 1.35 V vs NHE) [46], [47].

This study facilitated the separation between the charge carriers ($h^+ + e^-$), where formic acid performed multiple tasks. Its increased the photocatalytic capability of TiO_2 and produced reactive radicals, specifically $·CO_2^-$. The role of formic acid made it feasible for Cr(VI) to be effectively converted into Cr(III), which was seen from the experiment results. The reaction can be represented as follows [16].

$$TiO_2 + hv \rightarrow TiO_2 (h^+ + e^-) \tag{3}$$
$$h^+ + H_2O \rightarrow ·OH + H^+ \tag{4}$$
$$HCrO_4^- + 7H^+ + 3e^- \rightarrow Cr^{3+} + 4H_2O \tag{5}$$
$$Cr_2O_7^{2-} + 14H^+ + 6e^- \rightarrow 2Cr^{3+} + 7H_2O \tag{6}$$
$$HCOO^- + ·OH \rightarrow ·CO_2^- + H_2O \tag{7}$$
$$HCrO_4^- + ·CO_2^- + 7H^+ \rightarrow Cr^{3+} + CO_2 + 4H_2O \tag{8}$$
$$Cr_2O_7^{2-} + 3·CO_2^- + 14H^+ \rightarrow 2Cr^{3+} + 3CO_2 + 7H_2O \tag{9}$$

4.0 CONCLUSION

The photocatalytic reduction experiments of $TiO_2/NiSe/NC$ in water for Cr(VI) have been successfully conducted, employing various conditions such as lighting (no light, TL lamp, 365 nm lamp, 254 nm lamp) and the use of a hole scavenger (formic acid). Rutile TiO_2's bandgap has decreased from 3 eV to 2.87 eV. P25 TiO_2's bandgap has decreased from 3.14 eV to 3.04 eV. The photoreduction test indicated that the composite outperformed pure TiO_2. Under 254 nm light, the P25 sample showed a notable increase from 20.41% (P) to 53.26% (Pk). The Rk sample, which achieved a photoreduction rate of up to 48 %, shows the strongest activity in TL light, according to the research findings. This is explained by the 2.87 eV bandgap energy of the Rk sample. On the other hand, the Pk sample exhibits the most significant photoreduction rate when exposed to UV radiation, reaching 99.7 %. This finding is related to the selection of the TiO_2 precursor, more specifically, TiO_2 P25. Across all samples, formic acid is seen to enhance photoreduction activity significantly. As a result of the findings, it can be concluded that $TiO_2/NiSe/NC$ has the potential for use

and future development as a photocatalyst for reducing the heavy metal Cr (VI).

Conflicts of Interest

The author(s) declare(s) that there is no conflict of interest regarding the publication of this paper

References

[1]   M. Nasrollahzadeh, M. Sajjadi, S. Iravani, and R. S. Varma. 2021. Green-synthesized nanocatalysts and nanomaterials for water treatment: Current challenges and future perspectives. *Journal of Hazardous Materials*. 401: 123401. DOI: 10.1016/j.jhazmat.2020.123401.

[2]   N. Saha, M. S. Rahman, M. B. Ahmed, J. L. Zhou, H. H. Ngo, and W. Guo. 2017. Industrial metal pollution in water and probabilistic assessment of human health risk. *Journal of Environmental Management*. 185: 70–78. DOI: 10.1016/j.jenvman.2016.10.023.

[3]   M. Tumolo *et al.* 2020. Chromium Pollution in European Water, Sources, Health Risk, and Remediation Strategies: An Overview. *International Journal of Environmental Research and Public Health*. 17(15): 5438. DOI: 10.3390/ijerph17155438.

[4]   K. Brindha and M. Schneider. 2019. *GIS and Geostatistical Techniques for Groundwater Science*. Amsterdam: Elsevier. 179–196. DOI: 10.1016/B978-0-12-815413-7.00013-4.

[5]   A. Bakshi and A. K. Panigrahi. 2018. A comprehensive review on chromium induced alterations in fresh water fishes. *Toxicology Reports*. 5: 440–447. DOI: 10.1016/j.toxrep.2018.03.007.

[6]   V. Velma, S. S. Vutukuru, and P. B. Tchounwou. 2009. Ecotoxicology of Hexavalent Chromium in Freshwater Fish: A Critical Review. *Reviews on Environmental Health*. 24(2): 129–145. DOI: 10.1515/reveh.2009.24.2.129

[7]   Y. C. Zhang, J. Li, M. Zhang, and D. D. Dionysiou. 2011. Size-Tunable Hydrothermal Synthesis of SnS2 Nanocrystals with High Performance in Visible Light-Driven Photocatalytic Reduction of Aqueous Cr(VI). *Environmental Science & Technology*. 45(21): 9324–9331. DOI: 10.1021/es202012b.

[8]   M. M. Islam, A. A. Mohana, M. A. Rahman, M. Rahman, R. Naidu, and M. M. Rahman. 2023. A Comprehensive Review of the Current Progress of Chromium Removal Methods from Aqueous Solution. *Toxics*. 11(3): 252. DOI: 10.3390/toxics11030252.

[9]   Md. Nur-E-Alam, Md. A. S. Mia, F. Ahmad, and Md. M. Rahman. 2020. An overview of chromium removal techniques from tannery effluent. *Applied Water Science*. 10(9): 205. DOI: 10.1007/s13201-020-01286-0.

[10]   M. A. Irshad *et al.* 2023. Enhancing chromium removal and recovery from industrial wastewater using sustainable and efficient nanomaterial: A review. *Ecotoxicology and Environmental Safety* 263: 115231, DOI: 10.1016/j.ecoenv.2023.115231.

[11]   C. Zhang, H.-X. Ren, C.-Q. Zhong, and D. Wu. 2020. Biosorption of Cr(VI) by immobilized waste biomass from polyglutamic acid production. *Scientific Reports*, 10(1): 3705. DOI: 10.1038/s41598-020-60729-5.

[12]   R. Dong *et al.* 2019. Morphology-controlled fabrication of CNT@MoS2/SnS2 nanotubes for promoting photocatalytic reduction of aqueous Cr(VI) under visible light. *Journal of Alloys and Compounds*. 784: 282–292. DOI: 10.1016/j.jallcom.2019.01.032.

[13]   A. Lathe and A. M. Palve. 2023. A review: Engineered nanomaterials for photoreduction of Cr(VI) to Cr(III). *Journal of Hazardous*

Materials Advances. 12: 100333. DOI: 10.1016/j.hazadv.2023.100333.

[14] V. Loryuenyong, N. Jarunsak, T. Chuangchai, and A. Buasri. 2014. The Photocatalytic Reduction of Hexavalent Chromium by Controllable Mesoporous Anatase TiO2 Nanoparticles. *Advances in Materials Science and Engineering*. 2014: 1–8. DOI: 10.1155/2014/348427.

[15] A. Deng, S. Wu, J. Hao, H. Pan, M. Li, and X. Gao. 2022. Photocatalytic Removal of Cr(VI) by Thiourea Modified Sodium Alginate/Biochar Composite Gel. *Gels*. 8(5): 293. DOI: 10.3390/gels8050293.

[16] J. B. Islam, M. Furukawa, I. Tateishi, H. Katsumata, and S. Kaneco. 2019. Photocatalytic Reduction of Hexavalent Chromium with Nanosized TiO2 in Presence of Formic Acid. *ChemEngineering*. 3(2): 33. DOI: 10.3390/chemengineering3020033.

[17] N. Wang, L. Zhu, K. Deng, Y. She, Y. Yu, and H. Tang. 2010. Visible light photocatalytic reduction of Cr(VI) on TiO2 in situ modified with small molecular weight organic acids. *Applied Catalysis B: Environmental*. 95: 400–407. DOI: 10.1016/j.apcatb.2010.01.019.

[18] Y.-H. Chang and M.-C. Wu. 2019. Enhanced Photocatalytic Reduction of Cr(VI) by Combined Magnetic TiO2-Based NFs and Ammonium Oxalate Hole Scavengers. *Catalysts*. 9(1): 72. DOI: 10.3390/catal9010072.

[19] F. E. Bortot Coelho, V. M. Candelario, E. M. R. Araújo, T. L. S. Miranda, and G. Magnacca. 2020. Photocatalytic Reduction of Cr(VI) in the Presence of Humic Acid Using Immobilized Ce–ZrO2 under Visible Light. *Nanomaterials (Basel)*. 10(4): 779. DOI: 10.3390/nano10040779.

[20] A. Azizi and J. Saien. 2018. Optimization of Cr(VI) Photocatalytic Reduction by UV/TiO2 : Influence of Inorganic and Organic species and Kinetic Study. *Archives of Hygiene Sciences*. 7(2): 81–90. DOI: 10.29252/ArchHygSci.7.2.81.

[21] A. Kudo. 2007. Recent progress in the development of visible light-driven powdered photocatalysts for water splitting. *International Journal of Hydrogen Energy*. 32(14): 2673-2678. DOI: https://doi.org/10.1016/j.ijhydene.2006.09.010.

[22] Z. Wang, C. Li, and K. Domen. 2019. Recent developments in heterogeneous photocatalysts for solar-driven overall water splitting. *Chemical Society Reviews*. 48(7): 2109–2125. DOI: 10.1039/C8CS00542G.

[23] R. Zouzelka, Y. Kusumawati, M. Remzova, J. Rathousky, and T. Pauporté. 2016. Photocatalytic activity of porous multiwalled carbon nanotube-TiO2 composite layers for pollutant degradation. *Journal of Hazardous Materials*. 317: 52–59. DOI: 10.1016/j.jhazmat.2016.05.056.

[24] Y. Cong, B. Tian, and J. Zhang. 2011. Improving the thermal stability and photocatalytic activity of nanosized titanium dioxide via La3+ and N co-doping. *Applied Catalysis B: Environmental*. 101(3): 376–381, DOI: 10.1016/j.apcatb.2010.10.006.

[25] M. Ismael. 2020. A review and recent advances in solar-to-hydrogen energy conversion based on photocatalytic water splitting over doped-TiO2 nanoparticles. *Solar Energy*. 211: 522–546. DOI: 10.1016/j.solener.2020.09.073.

[26] M. Humayun, F. Raziq, A. Khan, and W. Luo. 2018. Modification strategies of TiO2 for potential applications in photocatalysis: a critical review. *Green Chemistry Letters and Reviews*. 11(2): 86–102. DOI: 10.1080/17518253.2018.1440324.

[27] H. Gong, Q. Liu, and C. Huang. 2019. NiSe as an effective co-catalyst coupled with TiO2 for enhanced photocatalytic hydrogen evolution. *International Journal of Hydrogen Energy*. 44(10): 4821–4831. DOI: 10.1016/j.ijhydene.2019.01.039.

[28] Y. Li, H. Wang, and S. Peng. 2014. Tunable Photodeposition of MoS2 onto a Composite of Reduced Graphene Oxide and CdS for Synergic Photocatalytic Hydrogen Generation. *The Journal of Physical Chemistry C.* 118(34): 19842–19848. DOI: 10.1021/jp5054474.

[29] P. Zhang, T. Wang, and H. Zeng. 2017. Design of Cu-Cu2O/g-C3N4 nanocomponent photocatalysts for hydrogen evolution under visible light irradiation using water-soluble Erythrosin B dye sensitization. *Applied Surface Science*. 391: 404–414. DOI: 10.1016/j.apsusc.2016.05.162.

[30] J. Ding, P. Wang, S. Ji, H. Wang, D. J. L. Brett, and R. Wang. 2019. Mesoporous nickel selenide N-doped carbon as a robust electrocatalyst for overall water splitting. *Electrochimica Acta*. 300: 93–101. DOI: 10.1016/j.electacta.2019.01.093.

[31] A. Haider, Z. N. Jameel, and Y. Taha. 2015. Synthesis and Characterization of TiO2 Nanoparticles via Sol- Gel Method by Pulse Laser Ablation. *Engineering and Technology Journal*. 33(5): 761-771.

[32] L. Mi *et al.* 2012. 3D hierarchically patterned tubular NiSe with nano-/microstructures for Li ion battery design. *Dalton Transactions.* 41: 12595-12600. DOI: 10.1039/c2dt31787g.

[33] M. Khan *et al.* 2021. Development and characterization of regenerable chitosan-coated nickel selenide nano-photocatalytic system for decontamination of toxic azo dyes. *International Journal of Biological Macromolecules*. 182: 866–878. DOI: 10.1016/j.ijbiomac.2021.03.192.

[34] Y. Kusumawati, M. A. Martoprawiro, and T. Pauporté. 2014. Effects of Graphene in Graphene/TiO2 Composite Films Applied to Solar Cell Photoelectrode. *The Journal of Physical Chemistry C*. 118(19): 9974–9981. DOI: 10.1021/jp502385p.

[35] A. B. D. Nandiyanto, R. Ragadhita, and M. Fiandini. 2023. Interpretation of Fourier Transform Infrared Spectra (FTIR): A Practical Approach in the Polymer/Plastic Thermal Decomposition. *Indonesian Journal of Science and Technology*. 8(1): 113-126. DOI: 10.17509/ijost.v8i1.53297.

[36] P. Praveen, G. Viruthagiri, S. Mugundan, and N. Shanmugam. 2014. Structural, optical and morphological analyses of pristine titanium di-oxide nanoparticles-Synthesized via sol-gel route. *Spectrochimica Acta Part A Molecular and Biomolecular Spectroscopy.* 117: 622–629. DOI: 10.1016/j.saa.2013.09.037.

[37] M. Sandhya, D. Ramasamy, K. Sudhakar, K. Kadirgama, and W. S. W. Harun. 2021. Ultrasonication an intensifying tool for preparation of stable nanofluids and study the time influence on distinct properties of graphene nanofluids – A systematic overview. *Ultrason Sonochem*. 73: 105479. DOI: 10.1016/j.ultsonch.2021.105479.

[38] D. A. H. Hanaor and C. C. Sorrell. 2011. Review of the anatase to rutile phase transformation. *Journal of Materials Science*. 46(4): 855–874. DOI: 10.1007/s10853-010-5113-0.

[39] A. Sclafani and J. M. Herrmann. 1996. Comparison of the Photoelectronic and Photocatalytic Activities of Various Anatase and Rutile Forms of Titania in Pure Liquid Organic Phases and in Aqueous Solutions. *The Journal of Physical Chemistry.* 100(32): 13655–13661. DOI: 10.1021/jp9533584.

[40] I. García-Sosa and M. Olguín. 2015. Comparison Between the Cr(VI) Adsorption by Hydrotalcite and Hydrotalcite-Gibbsite Compounds. *Separation Science and Technology*. 50(17): 2631–2638. DOI: 10.1080/01496395.2015.1066810.

[41] M. Gardner and S. Comber. 2002. Determination of trace concentrations of hexavalent chromium. *Analyst*. 127(1): 153–156. DOI: 10.1039/B109374F.

[42] G. Duffy, I. Maguire, B. Heery, P. Gers, J. Ducrée, and F. Regan. 2018. ChromiSense: A colourimetric lab-on-a-disc sensor for chromium speciation in water. *Talanta*. 178: 392–399. DOI: 10.1016/j.talanta.2017.09.066.

[43] A. Samad *et al.* 2017. Indirect Photocatalytic Reduction of Arsenate to Arsenite in Aqueous Solution with TiO 2 in the Presence of Hole Scavengers. *Chinese Journal of Chemical Engineering*. 26(3): 529-533. DOI: 10.1016/j.cjche.2017.05.019.

[44] H. Li, H. Yu, X. Quan, S. Chen, and H. Zhao. 2015. Improved Photocatalytic Performance of Heterojunction by Controlling the Contact Facet: High Electron Transfer Capacity between TiO2 and the 110 Facet of BiVO4 Caused by Suitable Energy Band Alignment. *Advanced Functional Materials*. 25(20): 3074–3080. DOI: 10.1002/adfm.201500521.

[45] J. Qin and H. Zeng. 2017. Photocatalysts fabricated by depositing plasmonic Ag nanoparticles on carbon quantum dots/graphitic carbon nitride for broad spectrum photocatalytic hydrogen generation. *Applied Catalysis B: Environmental*. 209: 161–173. DOI: 10.1016/j.apcatb.2017.03.005.

[46] Y. A. Shaban, A. A. El Maradny, and R. Kh. Al Farawati. 2016. Photocatalytic reduction of nitrate in seawater using C/TiO2 nanoparticles. *Journal of Photochemistry and Photobiology A: Chemistry*. 328: 114–121. DOI: 10.1016/j.jphotochem.2016.05.018.

[47] L. Wang *et al.* 2013. Efficient photocatalytic reduction of aqueous Cr(VI) over flower-like SnIn4S8 microspheres under visible light illumination. *Journal of Hazardous Materials*. 244–245: 681–688. DOI: 10.1016/j.jhazmat.2012.10.062.